Linear and nonlinear optical susceptibilities and hyperpolarizability of borate $LiNaB_4O_7$ single crystals: Theory and experiment

Ali Hussain Reshak,[1,2,a)] Xuean Chen,[3,b)] S. Auluck,[4] and H. Kamarudin[2]
[1]*School of Complex Systems, FFPW, CENAKVA-University of South Bohemia in CB, Nove Hrady 37333, Czech Republic*
[2]*School of Material Engineering, Malaysia University of Perlis, P.O. Box 77, d/a Pejabat Pos Besar, 01007 Kangar, Perlis, Malaysia*
[3]*College of Materials Science and Engineering, Beijing University of Technology, Ping Le Yuan 100, Beijing 100124, People's Republic of China*
[4]*National Physical Laboratory, Dr. K. S. Krishnan Marg, New Delhi 110012, India*

(Received 19 January 2012; accepted 9 August 2012; published online 13 September 2012)

$LiNaB_4O_7$ was synthesized by employing high-temperature reaction methods. The purity of the sample was checked by x-ray powder diffraction. The optical properties were measured by analyzing the diffuse reflectance data which showed a band gap of about 3.88 eV. Linear and nonlinear optical susceptibility calculations have been performed using the all-electron full potential linearized augmented plane wave method using four different exchange correlation potentials. It was found that the title compound possesses an optical gap of about 2.80 eV using the local density approximation, 2.91 eV by generalized gradient approximation, 3.21 eV for the Engel-Vosko generalized gradient approximation (EVGGA), and 3.81 eV using modified Becke-Johnson potential (mBJ). This compares well with our experimentally measured energy band gap of 3.88 eV. Our calculations show that EVGGA and mBJ cause a blue spectral shift with significant changes in the whole spectra. The observed spectral shifts are in agreement with the calculated band structure and corresponding electron density of states. The tensor $\chi^{(2)}_{ijk}$ describes the second-order nonlinear optical effect and the symmetry allows only five nonzero components, namely, the 113, 232, 311, 322, and 333 components with 322 being the dominant one with a value 0.15 pm/V ($d_{32} = 0.0733$ pm/V) at static limit and 0.16 pm/V ($d_{32} = 0.0795$ pm/V) at $\lambda = 1064$ nm. For the dominant component, the microscopic second order hyperpolarizability, β_{322}, was found to be 0.306×10^{-30} esu at static limit and 0.332×10^{-30} esu at $\lambda = 1064$ nm. © *2012 American Institute of Physics*. [http://dx.doi.org/10.1063/1.4749409]

I. INTRODUCTION

Borate materials have been extensively investigated because of their potential applications in nonlinear optics (NLO) and laser engineering and because they show excellent properties, such as short growth period, large effective nonlinear coefficient, high damage threshold, and good mechanical properties. For example, BaB_2O_4, LiB_3O_5, CsB_3O_5, and $YCa_4(BO_3)_3O$ are all well-known NLO crystals.[1] As a result of their complicated crystal structures borates are among the most interesting and therefore the most extensively studied materials. Since 1962, when the binary phase diagram Bi_2O_3–B_2O_3 was investigated, many methods of obtaining the borate crystals were found and described in detail.[2–7] In the Bi_2O_3–B_2O_3 system,[8] at least five compounds have been proposed and structurally characterized. They are $Bi_{24}B_2O_{39}$,[9] $Bi_4B_2O_9$,[10] $Bi_3B_5O_{12}$,[7] BiB_3O_6,[11] and $Bi_2B_8O_{15}$.[12] Among them, $Bi_4B_2O_9$ was reported to have high double refraction,[13] $Bi_3B_5O_{12}$ displays stimulated Raman scattering and luminescence properties.[14,15] BiB_3O_6 is the most extensively studied because it has been established as a NLO material with promising physical properties and has furthermore been characterized in detail with respect to their piezoelectric, pyroelectric, dielectric, elastic, and thermoelastic properties.[16] It was established that borate crystals, in particular BiB_3O_6, exhibit high NLO susceptibilities,[17–20] particularly for second harmonic generation (SHG) and third harmonic generation (THG) applications. Theoretical examinations have shown that anionic groups and chemical bonding structures of boron atoms have a major influence on the nonlinear properties of these crystals.[7,21] It is reasonable to emphasize that other interesting materials may also be found in more complex borates incorporating bismuth together with other cationic elements. Based on this idea, several ternary (quaternary) bismuth-containing borates that crystallize in the noncentrosymmetric space groups have been recently synthesized, including $BaBiBO_4$, $Bi_2ZnB_2O_7$, $CaBiGaB_2O_7$, $Bi_2CaB_2O_7$, and $Bi_2SrB_2O_7$.[22–24]

Further insight into the electronic structures and the physical properties of materials can be obtained from the calculations of interband optical functions. The considered compound is particularly interesting for its NLO properties, which could be related to the anionic and cationic polyhedral and to find such directions in which these materials may give large optical susceptibilities. Utilizing their anisotropy, there

a)Author to whom correspondence should be addressed. Electronic mail: maalidph@yahoo.com. Tel.: +420 777729583. Fax: +420-386 361255.
b)E-mail address: xueanchen@bjut.edu.cn.

appears a possibility to increase the corresponding optical susceptibilities. Moreover, by inducing changes in the cationic sub-systems one can also vary the transparency and mechanical properties. Thus, one requires reliable information about the optical functions.

In the course of our investigation of novel borate NLO materials, we have obtained single crystals of $LiNaB_4O_7$. Our x-ray structural analysis has revealed that $LiNaB_4O_7$ crystallizes in the orthorhombic noncentrosymmetric space group F*dd*2, with unit cell parameters $a = 13.326(3)$ Å, $b = 14.072(3)$ Å, $c = 10.238(2)$ Å, $Z = 16$, and $V = 1919.9(7)$ Å^3. Although the crystal structure of this compound has been previously determined,[25] one of the lattice constant was wrong (c = 10.7243(2) Å, Table I, Ref. 25) and the Crystallographic Information File (CIF) file deposited in Inorganic Crystal Structure Database (ICSD) is also incorrect. Here, we give the correct cell dimensions in this work. Moreover, no first principle calculations on the electronic structure and linear and nonlinear optical susceptibilities of $LiNaB_4O_7$ are available in the literature. As natural extension to our experimental research work, we addressed ourselves to support our experimental results through the first principle calculations based on the state-of-the-art full potential linear augmented plane wave (FPLAPW) method to calculate the linear and nonlinear optical susceptibilities. In our previous work, we have shown that the FP-LAPW method has proved to be one of the most accurate methods for the reproduction of electronic structure of solids within density functional theory (DFT).[26,27] In this work, we report results of the experimental measurements mentioned above and theoretical calculations so as to make a meaningful comparison.

II. METHODOLOGY

A. Synthesis and x-ray crystallography

The title compound was synthesized by employing high-temperature solution reaction methods. All reagents were of analytical grade. For the preparation of $LiNaB_4O_7$ crystals, a powder mixture of 3.5936 g Na_2CO_3, 3.1776 g Ga_2O_3, 8.3854 g H_3BO_3, and 2.8670 g $Li_2B_4O_7$ ($Na_2CO_3/Ga_2O_3/H_3BO_3/Li_2B_4O_7$ molar ratio = 2:1:8:1) was transferred to a 40 ml Pt crucible. The sample was gradually heated to 840 °C, where it was kept for two weeks, then cooled down to 810 °C at a rate of 1.0 °C/h, and to 600 °C at a rate of 5.0 °C/h, followed by cooling to room temperature at a rate of 20 °C/h. The colorless, prismatic crystals of $LiNaB_4O_7$ were observed on the surface regions of the sample contacting the wall of the Pt crucible. Several small crystals were recovered and mechanically separated from the reaction product. Energy-dispersive x-ray analysis in a scanning electron microscope confirmed the presence of sodium as the only heavy element. Although Ga was not incorporated into the final structure, Ga_2O_3 acted as a flux for the crystal growth. Subsequently, direct reaction of a stoichiometric mixture of $Li_2B_4O_7$ and $Na_2B_4O_7{\cdot}10H_2O$ at 630 °C for four weeks with several intermediate grindings yielded a single-phase polycrystalline sample as identified by powder XRD analyses. This compound is relatively stable in air and water, but soluble in hot diluted HNO_3 solution.

TABLE I. Crystallographic data for $LiNaB_4O_7$.

Formula	$LiNaB_4O_7$
Space group	*F d d* 2 (*No.* 43)
a (Å)	13.326(3)
b (Å)	14.072(3)
c (Å)	10.238(2)
V (Å^3), *Z*	1919.9(7), 16
d_{calc} (g/cm^3)	2.563
μ (mm^{-1})	0.310
$2\theta_{max}$ (°)	59.9
Unique reflection	730
Observed [$I \geq 2\sigma(I)$]	715
No. of variables	120
GOF on F_o^2	1.167
R1/*wR2* [$I \geq 2\sigma(I)$]	0.0327/0.0954
R1/*wR2* (all data)	0.0333/0.0955

Single-crystal x-ray intensity data were collected at room temperature (290 K) on an automated Rigaku AFC7R four-circle diffractometer using monochromatized Mo Kα radiation ($\lambda = 0.71073$ Å). Cell dimensions were first obtained from a least-squares refinement with 25 automatically centered reflections. Subsequently, searching in ICSD (Inorganic Crystal Structure Database) indicates that the cell dimensions are different from those of the known borate crystalline phases; therefore, the intensity data are further collected. The data were corrected for Lorentz and polarization effects, and for absorption by empirical method based on Ψ-scan data. The crystal structure was solved by a direct method and refined in SHELX-97 system[28] by full-matrix least-squares methods on F_O^2. After introduction of anisotropic displacement parameters for all atoms, the refinement of 120 parameters with 715 observed reflections [$I \geq 2\sigma(I)$] resulted in the residuals of *R1*/*wR2* = 0.0327/0.0954. Refinements produced the formula of this compound, $LiNaB_4O_7$. This phase has been previously reported;[27] however, one of lattice constant given by Maczka *et al.*[25] is wrong and the CIF file deposited in ICSD is also incorrect, and we used the correct cell dimensions in this work. Details of crystal parameters, data collection, and structure refinements are given in Table I, atomic coordinates and equivalent isotropic displacement parameters are summarized in Table II. All these parameters are summarized in the new CIF.

The basic structural unit in $LiNaB_4O_7$ is a $[B_4O_9]^{6-}$ group that consists of two vertex-sharing BO_4 tetrahedra and two bridging BO_3 triangles, as shown in Fig. 1(a). Each $[B_4O_9]^{6-}$ group is linked to four other similar groups through sharing the nonbridging O atoms to form a three-dimensional (3D) $^3_\infty[B_4O_7]^{2-}$ network. There are two independent and interpenetrating 3D $^3_\infty[B_4O_7]^{2-}$ frameworks in this structure: one composed of B1, B2, O1, O2, O3, and O4 atoms and another formed by the rest of B and O atoms. The 3D

TABLE II. Atomic coordinates and equivalent isotropic displacement parameters (Å^2) for $LiNaB_4O_7$. U_{eq} is defined as one third of the trace of the orthogonalized **U** tensor.

Atoms	X	Y	Z	U_{eq}
Li1	0.0047(5)	0.3569(7)	0.1220(8)	0.040(2)
Na1	0.10116(11)	0.23889(10)	0.37457(16)	0.0244(4)
B1	0.1646(2)	0.22276(18)	0.0797(3)	0.0073(5)
B2	0.0447(2)	0.1219(2)	−0.0521(3)	0.0091(5)
B3	0.2153(2)	0.17260(19)	0.5971(3)	0.0066(5)
B4	0.1264(2)	0.0443(2)	0.4655(3)	0.0072(5)
O1	0.07228(15)	0.20174(14)	0.0105(2)	0.0119(4)
O2	0.2500	0.2500	−0.0025(3)	0.0106(5)
O3	0.19556(15)	0.14068(14)	0.1644(2)	0.0133(4)
O4	0.13551(15)	0.30374(14)	0.1680(2)	0.0116(4)
O5	0.20520(13)	0.08226(14)	0.5287(2)	0.0100(4)
O6	0.2500	0.2500	0.5145(3)	0.0079(5)
O7	0.29022(15)	0.15260(14)	0.7021(2)	0.0096(4)
O8	0.11986(14)	0.20357(14)	0.6642(2)	0.0091(4)

framework affords intersecting channels running parallel to [100] and [010] direction that are selectively occupied by Na^+ and Li^+ cations, respectively.

B. Experimental optical properties

In order to investigate the band-gap energy and the band structure, experiments were conducted to measure the optical diffuse reflectance spectra of $LiNaB_4O_7$ at room temperature using a Shimadzu UV-3101PC double-beam, double-monochromator spectrophotometer. Data were collected in the wavelength range 200–900 nm. $BaSO_4$ powder was used as a standard (100% reflectance). A similar procedure as previously described[29,30] was used to collect and convert the data using the Kubelka-Munk function $F(R) = (1-R)^2/2R$, where R is the reflectance. The minima in the second-derivative curves of the Kubelka-Munk function are taken as the position of the absorption bands.

The optical diffuse reflectance spectrum is shown in Fig. 2. It is clear that no significant absorption peaks were observed above 400 nm, implying that the material is transparent under the visible light. A strong absorption peak appears at around 240 nm (5.17 eV). The absorption edge of UV-vis diffuse reflectance spectrum is at around 320 nm, from which the optical band gap is estimated to be roughly 3.88 eV. The calculated absorption coefficient, presented at Fig. 2, shows the fundamental optical absorption peak located at 230 nm using modified Becke-Johnson potential (mBJ) in good agreement with the experimental data where the peaks occurs at 240 nm. The second peak in the calculation at around 280 nm is absent in the experimental data due to broadening resulting from temperature, impurities, and experimental. We should emphasize that the calculated absorption coefficient agrees well with the measured optical diffuse reflectance spectrum in the matter of showing a very sharp rise at low wavelengths and a very low absorption in the UV-vis region at wavelengths greater than 320–340 nm. It is pertinent to mention that electron-hole interactions play a very important role in the optical properties. In particular, the presence of excitons in the sample will result in an energy gap that is smaller than the real/actual energy gap. This must be taken into account

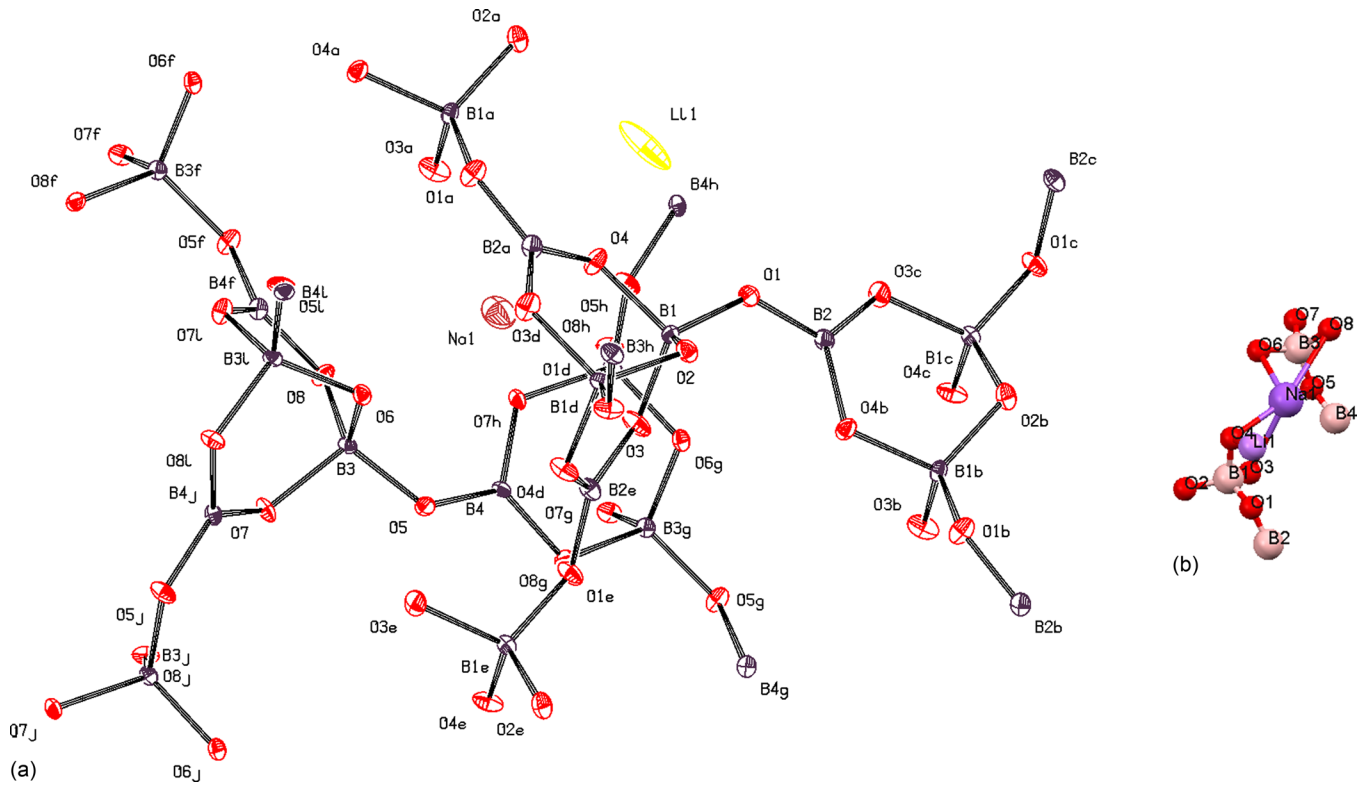

FIG. 1. (a) Fragment of the crystal structure of $LiNaB_4O_7$ with the atomic labeling scheme. (b) Asymmetric unit of $LiNaB_4O_7$.

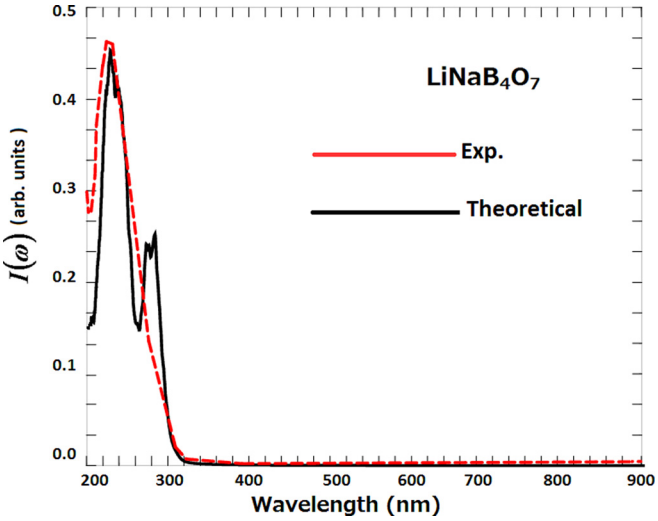

FIG. 2. Measured optical absorption spectrum of $LiNaB_4O_7$ (absorption coefficient is in arbitrary units) along with calculated absorption spectrum $I(\omega)$ using mBJ (absorption coefficient is in arbitrary units).

when one compares the calculated energy gap with the experimental energy gap as deduced from the absorption spectrum.

C. Details of theoretical calculation

We have performed first principle calculations based on the state-of-the-art all-electron FP-LAPW method to solve the Kohn Sham DFT equations within the framework of the WIEN2K code.[31] This is an implementation of the DFT[32] with different possible approximation for the exchange correlation (XC) potentials. Exchange and correlation potential is described by the local density approximation (LDA) of Ceperley-Alder (CA)[33] and the generalized gradient approximation (GGA),[34] which are based on exchange-correlation energy optimization to calculate the total energy. In addition, the Engel-Vosko generalized gradient approximation (EV-GGA)[35] and mBJ[36] were also employed to avoid the well-known LDA and GGA underestimation of the band gaps. The Kohn-Sham equations are solved using a basis of linear APW's. The potential and charge density in the muffin-tin (MT) spheres are expanded in spherical harmonics with $l_{max} = 8$ and nonspherical components up to $l_{max} = 6$. In the interstitial region, the potential and the charge density are represented by Fourier series. The atomic positions taken from our XRD data were optimized by minimization of the forces (1 mRy/au) acting on the atoms (see Table III). From the relaxed geometry, the electronic structure and the chemical bonding can be determined and various spectroscopic features can be simulated and compared with experimental data. Once the forces are minimized in this construction, one can then find the self-consistent density at these positions by turning off the relaxations and driving the system to self-consistency. The self-consistent calculations are converged since the total energy of the system is stable within 10^{-5} Ry. Self-consistency is obtained using 200 $\vec{k}$ points in the irreducible Brillouin zone (IBZ). The linear and nonlinear optical susceptibilities are calculated using 1200 **k**-points in the IBZ.

TABLE III. Optimized atomic coordinates for $LiNaB_4O_7$.

Atoms	X	Y	Z
Li	0.00238(5)	0.36781(4)	0.12989(3)
Na	0.10427(2)	0.23886(9)	0.37393(3)
B1	0.16279(9)	0.22468(2)	0.07839(1)
B2	0.04335(2)	0.12233(3)	0.94579(5)
B3	0.21617(1)	0.17204(1)	0.59814(4)
B4	0.12744(9)	0.04277(1)	0.46556(1)
O1	0.07048(6)	0.20347(9)	0.00870(6)
O2	0.2500	0.2500	0.99439(9)
O3	0.19371(1)	0.14287(1)	0.16518(5)
O4	0.13394(5)	0.30628(6)	0.16443(2)
O5	0.20746(8)	0.08165(5)	0.52852(2)
O6	0.2500	0.2500	0.51399(1)
O7	0.29096(6)	0.15337(2)	0.70383(6)
O8	0.11931(9)	0.20184(6)	0.66456(9)

III. RESULTS AND DISCUSSION

A. Linear optical susceptibilities

Further insight into the electronic structure can be obtained from the calculation of interband optical functions. $LiNaB_4O_7$ crystallizes in the space group $F\ d\ d\ 2$ (*No.* 43). This symmetry allows three non-zero components of the dielectric (optical) tensor corresponding to the electric field $\vec{E}$ being directed along **a**, **b**, and **c**-crystallographic axes. This single crystal possesses well pronounced structures for the three principal complex tensor components; $\varepsilon^{xx}(\omega)$, $\varepsilon^{yy}(\omega)$, and $\varepsilon^{zz}(\omega)$. The imaginary part of the three principal complex tensor components completely defines the linear optical susceptibilities. The imaginary part of the three principal complex tensor components represents the direct inter-band transitions between valence (VB) and conduction band (CB) states. According to the dipolar selection rule, only transitions changing the angular momentum quantum number l by unity are allowed. The imaginary parts $\varepsilon_2^{xx}(\omega)$, $\varepsilon_2^{yy}(\omega)$, and $\varepsilon_2^{zz}(\omega)$ of the optical function's dispersion were calculated using the traditional expression:[37]

$$\varepsilon_2^{ij}(\omega) = \frac{8\pi^2\hbar^2e^2}{m^2V}\sum_k\sum_{cv}(f_c - f_v)\frac{p_{cv}^i(k)p_{vc}^j(k)}{E_{vc}^2} \times \delta[E_c(k) - E_v(k) - \hbar\omega], \quad (1)$$

where m, e, and $\hbar$ are the electron mass, charge, and Plank's constant, respectively. f_c and f_v represent the Fermi distributions of the conduction and valence bands, respectively. The term $p_{cv}^i(k)$ denotes the momentum matrix element transition from the energy level c of the conduction band to the level v of the valence band at certain **k**-point in the BZ and V is the unit cell volume. In order to show the effect of LDA, GGA, EVGGA, and mBJ on the optical dielectric constants, we have calculated the average $\varepsilon_2^{average}(\omega)$ value of $\varepsilon_2^{xx}(\omega)$, $\varepsilon_2^{yy}(\omega)$, and $\varepsilon_2^{zz}(\omega)$ as shown in Fig. 3(a), using the expression:[38]

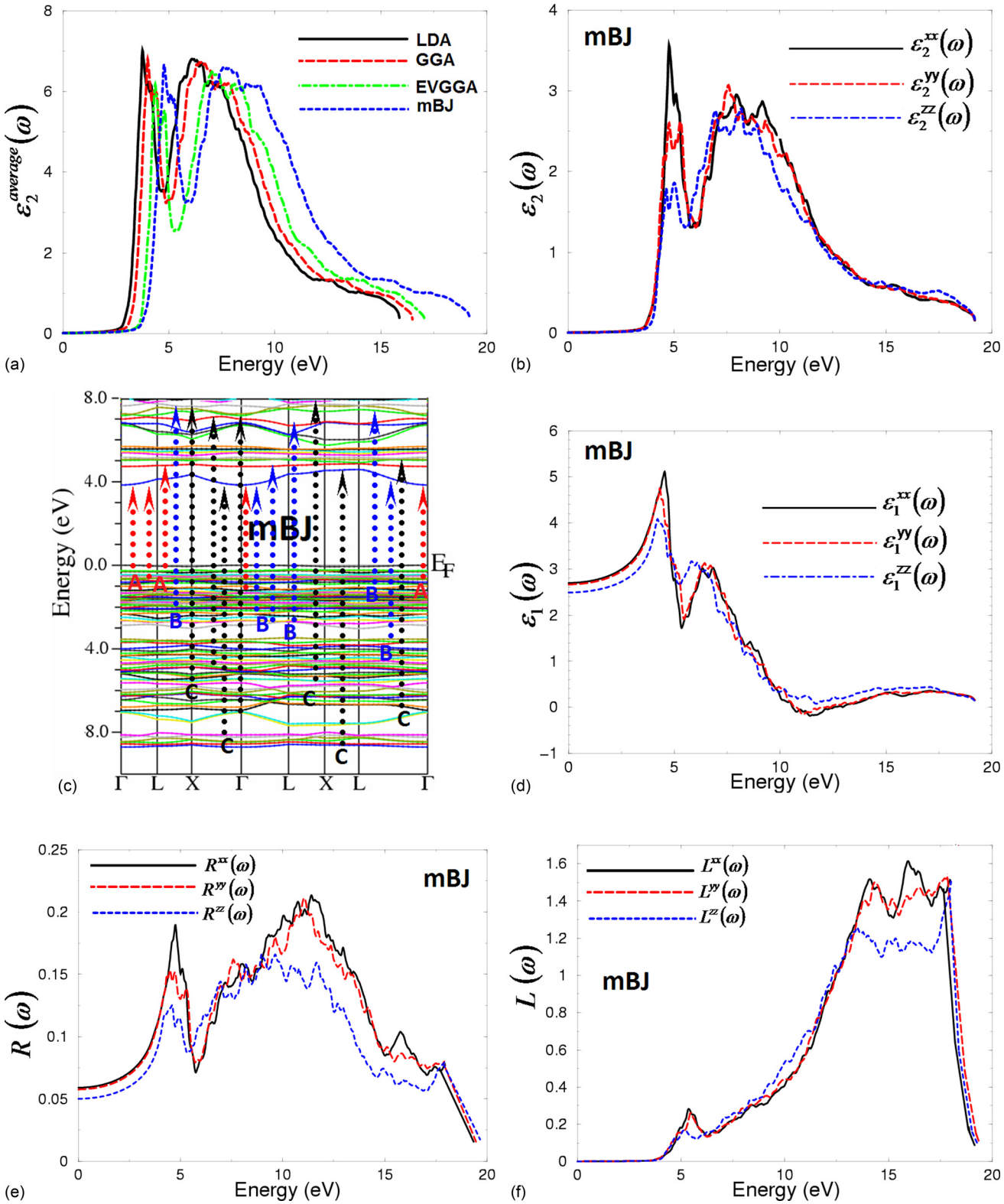

FIG. 3. (a) Calculated $\varepsilon_2^{average\_LDA}(\omega)$ (dark solid curve-black), $\varepsilon_2^{average\_GGA}(\omega)$ (light dashed curve-red), and $\varepsilon_2^{average\_EVGGA}(\omega)$ (light dotted dashed curve-blue) dispersion spectra. (b) Calculated $\varepsilon_2^{xx}(\omega)$ (dark solid curve-black), $\varepsilon_2^{yy}(\omega)$ (light dashed curve-red), and $\varepsilon_2^{zz}(\omega)$ (light dotted dashed curve-blue) dispersion spectra: mBJ with scissors correction. (c) The optical transitions depicted on a generic band structure. (d) Calculated $\varepsilon_1^{xx}(\omega)$ (dark solid curve-black), $\varepsilon_1^{yy}(\omega)$ (light dashed curve-red), and $\varepsilon_1^{zz}(\omega)$ (light dotted dashed curve-blue) spectra using mBJ with scissors correction. (e) Calculated $R^{xx}(\omega)$ (dark solid curve-black), $R^{yy}(\omega)$ (light dashed curve-red), and $R^{zz}(\omega)$ (light dotted dashed curve-blue) using mBJ with scissors correction. (f) Calculated electron loss function $L^{xx}(\omega)$ (dark solid curve-back), $L^{yy}(\omega)$ (light dashed curve-red), and $L^{zz}(\omega)$ (light dotted dashed curve-blue) spectrum using mBJ with scissors correction. (g) Calculated refractive indices $n^{xx}(\omega)$ (dark solid curve-black), $n^{yy}(\omega)$ (light dashed curve-red), and $n^{zz}(\omega)$ (light dotted dashed curve-blue) spectrum using mBJ with scissors correction.

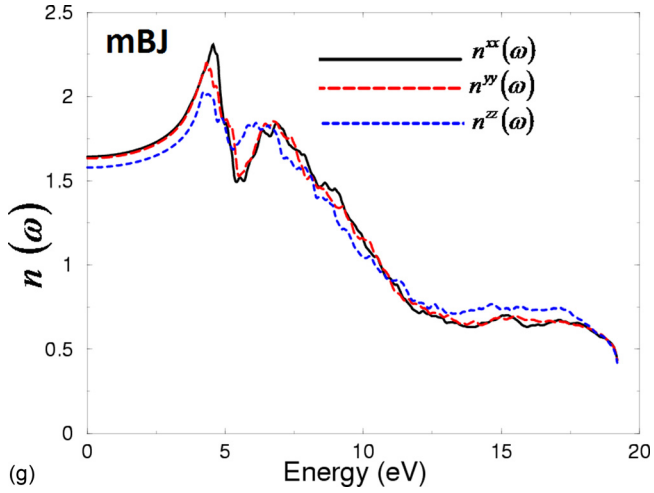

FIG. 3. (*Continued.*)

$$\varepsilon_2^{average}(\omega) = \frac{\varepsilon_2^{xx} + \varepsilon_2^{yy} + \varepsilon_2^{zz}}{3}. \quad (2)$$

Our calculations show that EVGGA and mBJ cause a blue spectral shift with significant changes in the whole spectra. The observed spectral shifts are in agreement with the calculated band structure and corresponding electron density of states. The fundamental optical absorption edges for $\varepsilon_2^{average}(\omega)$ are 2.8, 2.91, 3.21, and 3.81 eV for LDA, GGA, EVGGA, and mBJ, respectively. These edges of optical absorption give the threshold for direct optical transitions between the top of valence band and bottom of conduction band. The difference in the values of the absorption edge is attributed to the fact that the well-known LDA and GGA underestimate the band gaps. This is mainly due to the fact that LDA and GGA are based on simple model assumptions which are not sufficiently flexible to reproduce sufficiently the exchange correlation energy and its charge space derivative. The EVGGA approach is able to reproduce better exchange potential at the expense of less agreement in the exchange energy and yields better band splitting than those of LDA and GGA. The mBJ allows the calculation of band gaps with accuracy similar to the very expensive GW calculations.[36] It is a local approximation to an atomic "exact-exchange" potential and a screening term. As mBJ brings the optical gap close to our measured one, we select to show the calculated optical constants with mBJ.

Fig. 3(b) shows the calculated $\varepsilon_2^{xx}(\omega)$, $\varepsilon_2^{yy}(\omega)$, and $\varepsilon_2^{zz}(\omega)$ with mBJ. The optical constants are very anisotropic. We should emphasize that this anisotropy in the linear optical susceptibilities favors an enhanced phase matching conditions necessary for observation of the SHG and optical parametric oscillation (OPO). Following this figure, one can see that at low energies between 3.81 and 5.0 eV and higher energies between 8.0 and 11.0 eV the component $\varepsilon_2^{xx}(\omega)$ is dominant. While at energetic range 6.0–7.0 eV, the component $\varepsilon_2^{zz}(\omega)$ is dominant, and from 7.0 to 8.0 eV $\varepsilon_2^{yy}(\omega)$ is the dominant. The tail shows all components are isotropic. Generally, the spectral peaks in the optical functions are determined by the electric-dipole transitions between the occupied valance band states and the unoccupied conductions bands. These peaks can be identified from the calculated band structure. In order to identify these peaks, we need to look at the optical transition dipole matrix elements. We have analyzed the optical constant dispersion of $\varepsilon_2^{xx}(\omega)$, $\varepsilon_2^{yy}(\omega)$, and $\varepsilon_2^{zz}(\omega)$. We have established that the transitions which are responsible for the structures below 5 eV in $\varepsilon_2^{xx}(\omega)$, $\varepsilon_2^{yy}(\omega)$, and $\varepsilon_2^{zz}(\omega)$ spectra are prevailingly caused by transitions from sub-bands situated below Fermi energy (E_F) to bands just above it (see Fig. 3(c)). Whereas the transitions, which are responsible for the structures above 5 eV in $\varepsilon_2^{xx}(\omega)$, $\varepsilon_2^{yy}(\omega)$, and $\varepsilon_2^{zz}(\omega)$, originate from transitions between top/bottom of occupied Li-s/p, Na-s/p, O-s/p, and B-s/p sub-band states to the top/bottom of unoccupied Li-s/p, Na-s/p, O-s/p, and B-s/p states. We have used our calculated band structure to indicate the inter-band transitions, indicating the major structure for the principal components in the band structure diagram as A (3.81–5.0 eV), B (5.0–10.0 eV), and C (10.0–14.0 eV). The optical transitions depicted on a generic band structure in the vicinity of the fundamental absorption edge are illustrated in Fig. 3(c). These transitions are labeled according to the spectral peak positions in Fig. 3(b). For simplicity, we show only the transitions which are responsible for the principle spectral structures.

The real parts $\varepsilon_1^{xx}(\omega)$, $\varepsilon_1^{yy}(\omega)$, and $\varepsilon_1^{zz}(\omega)$ spectra are obtained using the Kramers-Kronig (KK) relations:[38]

$$\varepsilon_1(\omega) = 1 + \frac{2}{\pi} P \int_0^{\infty} \frac{\omega' \varepsilon_2(\omega')}{\omega'^2 - \omega^2} d\omega', \quad (3)$$

where P implies the principal value of the integral. The KK dispersion analysis is used to determine the complex conjugate variable. Fig. 3(d) shows $\varepsilon_1^{xx}(\omega)$, $\varepsilon_1^{yy}(\omega)$, and $\varepsilon_1^{zz}(\omega)$ optical function's dispersion. The calculated $\varepsilon_1^{xx}(0)$, $\varepsilon_1^{yy}(0)$, and $\varepsilon_1^{zz}(0)$ optical functions are 2.76, 2.73, and 2.44, respectively.

The reflectivity spectra along x-, y-, and z-axis are depicted in Fig. 3(e). The obtained reflectivity spectra show that at low energies the reflectivity spectrum started at around 0.05 then rapidly rise to reach first reflectivity

maximum at 5.0 eV. The highest first peak is for x-component of around 0.18. A valley-like occurs at 6.0 eV. A second reflectivity maximum occurs around 12.5 eV. The first reflectivity maximum and the valley-like are formed by inter-band transitions between p-states of VB and p-states of CB. The second reflectivity maximum is formed by inter-band transitions between s-states of VB to p-states of CB. The reflectivity spectrum reproduces well the spectral positions of the peaks determined by inter-band transitions with high accuracy. It is interesting that there is an abrupt reduction in the reflectivity spectrum at energy about 17.5 eV correlating with the occurrence of a collective plasmon resonance. The depth of the plasmon minimum is determined by the imaginary part of the dielectric function at the plasma resonance and is representative of the degree of overlap between the inter-band absorption regions.

The energy loss function (ELF) represents the response of a material to fast electron traveling through it. The relation between the dielectric function and ELF can be written as[39]

$$\mathrm{ELF}\,(E) = \mathrm{Im}\left(\frac{-1}{\varepsilon(E)}\right) = \frac{\varepsilon_2}{\varepsilon_1^2 + \varepsilon_2^2}. \tag{4}$$

The spectrum of energy loss function is illustrated in Fig. 3(f). There are other features in this spectrum, in addition to the plasmon peak, associated with inter-band transitions. The plasmon peak usually occurs at energy where real part of the frequency dependent dielectric functions crosses zero. The energy of the maximum peak is observed between 7.5 and 17.5 eV which are assigned to the appearance of volume plasmon $\hbar\omega_p$. The plasmon losses corresponding to a collective oscillation of the valence electrons and their energies are closely related to the density of valence electrons. In the case of inter-band transitions, which consist mostly of plasmon excitations, the scattering probability for volume losses is directly connected to the energy loss function.

The calculated refractive index dispersions are shown in Fig. 3(g). Following this figure, we note that at 4.5 eV the crystal shows highest refractive indices and with the continuous increasing energies starts to decrease.

The calculated values of $n^{xx}(0)$, $n^{yy}(0)$, and $n^{zz}(0)$ are 1.642, 1.632, and 1.578, respectively. The birefringence can be calculated from the linear response functions from which the anisotropy of the index of refraction is determined. The birefringence is the difference between the extraordinary and the ordinary refraction indices, $\Delta n(\omega) = n_e(\omega) - n_o(\omega)$, where $n_o(\omega)$ is the index of refraction for an electric field oriented along the **c**-axis and $n_e(\omega)$ is the index of refraction for an electric field perpendicular to the **c**-axis. It is clear that the birefringence is crucial only in the non-absorbing spectral range, which is below the energy gap. Since $n^{xx}(0)$ and $n^{yy}(0)$ are almost same, we take the mean to be a good representative for $n_o(\omega)$ and $n^{zz}(0)$ to be $n_e(\omega)$. Thus, this crystal possesses a negative birefringence at zero energy equal to about −0.06.

B. Nonlinear optical susceptibilities

The following equation describes the normal nonlinear optical effect:

$$p_i = p_{0,i} + \alpha_0\left(\chi_{ij}^{(1)}E_j + \chi_{ijk}^{(2)}E_jE_k + \chi_{ijkl}^{(3)}E_jE_kE_l + \cdots\right), \tag{5}$$

p_0 is the spontaneous polarization, $\chi^{(n)}$ is the nth order susceptibility tensor, α_0 is the vacuum permittivity, and E is the applied electric field.

The complex second-order nonlinear optical susceptibility tensor $\chi_{ijk}^{(2)}(-2\omega;\omega;\omega)$ can be generally written as:[40–43]

$$\chi_{inter}^{ijk}(-2\omega;\omega,\omega) = \frac{e^3}{\hbar^2}\sum_{nml}\int\frac{d\vec{k}}{4\pi^3}\frac{\vec{r}_{nm}^{\,i}\{\vec{r}_{ml}^{\,j}\vec{r}_{ln}^{\,k}\}}{(\omega_{ln}-\omega_{ml})}\left\{\frac{2f_{nm}}{(\omega_{mn}-2\omega)}+\frac{f_{ml}}{(\omega_{ml}-\omega)}+\frac{f_{ln}}{(\omega_{ln}-\omega)}\right\}, \tag{6}$$

$$\begin{aligned}\chi_{intra}^{ijk}(-2\omega;\omega,\omega) = \frac{e^3}{\hbar^2}\int\frac{d\vec{k}}{4\pi^3}\Bigg[&\sum_{nml}\omega_{nm}\vec{r}_{nm}^{\,i}\{\vec{r}_{ml}^{\,j}\vec{r}_{ln}^{\,k}\}\left\{\frac{f_{nl}}{\omega_{ln}^2(\omega_{ln}-\omega)}-\frac{f_{lm}}{\omega_{ml}^2(\omega_{ml}-\omega)}\right\}\\ &-8i\sum_{nm}\frac{f_{nm}\vec{r}_{nm}^{\,i}\{\Delta_{mn}^{j}\vec{r}_{nm}^{\,k}\}}{\omega_{mn}^2(\omega_{mn}-2\omega)}+2\sum_{nml}\frac{f_{nm}\vec{r}_{nm}^{\,i}\{\vec{r}_{ml}^{\,j}\vec{r}_{ln}^{\,k}\}(\omega_{ml}-\omega_{ln})}{\omega_{mn}^2(\omega_{mn}-2\omega)}\Bigg],\end{aligned} \tag{7}$$

$$\chi_{\mathrm{mod}}^{ijk}(-2\omega;\omega,\omega) = \frac{e^3}{2\hbar^2}\int\frac{d\vec{k}}{4\pi^3}\left[\sum_{nml}\frac{f_{nm}}{\omega_{mn}^2(\omega_{mn}-\omega)}\{\omega_{nl}\vec{r}_{lm}^{\,i}\{\vec{r}_{mn}^{\,j}\vec{r}_{nl}^{\,k}\}-\omega_{lm}\vec{r}_{nl}^{\,i}\{\vec{r}_{lm}^{\,j}\vec{r}_{mn}^{\,k}\}\}-i\sum_{nm}\frac{f_{nm}\vec{r}_{nm}^{\,i}\{\vec{r}_{mn}^{\,j}\Delta_{mn}^{k}\}}{\omega_{mn}^2(\omega_{mn}-\omega)}\right]. \tag{8}$$

From these formulae, we can notice that there are three major contributions to $\chi_{ijk}^{(2)}(-2\omega;\omega;\omega)$: the inter-band transitions $\chi_{inter}^{ijk}(-2\omega;\omega,\omega)$, the intra-band transitions $\chi_{intra}^{ijk}(-2\omega;\omega,\omega)$, and the modulation of inter-band terms by

intra-band terms $\chi^{ijk}_{\mathrm{mod}}(-2\omega;\omega,\omega)$, where $n \neq m \neq l$. Here, n denotes the valence states, m the conduction states, and l denotes all states $(l \neq m,n)$. There are two kinds of transitions take place: one of them vcc', involves one valence band (v) and two conduction bands (c and c'), and the second transition $vv'c$, involves two valence bands (v and v') and one conduction band (c). The symbols are defined as $\Delta^i_{nm}(\vec{k}) = \vartheta^i_{nn}(\vec{k}) - \vartheta^i_{mm}(\vec{k})$ with $\vec{\vartheta}^i_{nm}$ being the i component of the electron velocity given as $\vartheta^i_{nm}(\vec{k}) = i\omega_{nm}(\vec{k})r^i_{nm}(\vec{k})$ and $\{r^i_{nm}(\vec{k})r^j_{ml}(\vec{k})\} = \frac{1}{2}\left(r^i_{nm}(\vec{k})r^j_{ml}(\vec{k}) + r^j_{nm}(\vec{k})r^i_{ml}(\vec{k})\right)$. The position matrix elements between band states n and m, $r^i_{nm}(\vec{k})$, are calculated from the momentum matrix element P^i_{nm} using the relation:[44] $r^i_{nm}(\vec{k}) = \frac{P^i_{nm}(\vec{k})}{im\omega_{nm}(\vec{k})}$, with the energy difference between the states n and m given by $\hbar\omega_{nm} = \hbar(\omega_n - \omega_m)$. $f_{nm} = f_n - f_m$ is the difference of the Fermi distribution functions. i, j, and k correspond to Cartesian indices.

It has been demonstrated by Aspnes[45] that only the one-electron virtual transitions (transitions between one valence band state and two conduction band states) give a significant contribution to the second-order tensor. We ignore the virtual-hole contribution (transitions between two valence band states and one conduction band state) because it was found to be negative and more than an order of magnitude smaller than the virtual-electron contribution for this compound. For simplicity, we denote $\chi^{(2)}_{ijk}(-2\omega;\omega;\omega)$ by $\chi^{(2)}_{ijk}(\omega)$. The subscripts i, j, and k are Cartesian indices. The formalisms for calculating the second order susceptibility $\chi^{(2)}_{ijk}(-2\omega;\omega;\omega)$ for non-magnetic semiconductors and insulators based on the FP-LAPW method have been presented in Refs. 40–43.

The tensor $\chi^{(2)}_{ijk}$ describes the second-order nonlinear optical effect. It is third rank tensor, in the electric dipole approximation, containing nonvanishing elements only for noncentrosymmetric crystalline structure. The third order nonlinear optical effects are described by the tensors $\chi^{(3)}_{ijkl}$ and γ_{ijkl} and no symmetry requirements are imposed on these effects to occur.[46] The space group $F\,d\,d\,2$ (*No.* 43) possesses two crystallographic symmetry elements and as a consequence we have several parameters which are equal to zero. As a result, the symmetry will allow only five nonzero components, namely, the 113, 232, 311, 322, and 333 components (1, 2, and 3 refer to the x, y, and z axes, respectively).[47] The calculated $|\chi^{(2)}_{ijk}(0)|$ and $|\chi^{(2)}_{ijk}(\omega)|$ at $\lambda = 1064$ nm for all the five tensor components are evaluated and listed in Table IV. The static values of the second order susceptibility tensor are very important and can be used to estimate the relative SHG efficiency. The calculated $|\chi^{(2)}_{ijk}(\omega)|$ for all components show that the 322 component is dominate one since it shows the highest value of $|\chi^{(2)}_{ijk}(\omega)|$ at both of static limit and at $\lambda = 1064$ nm among the others as illustrated in Fig. 4(a) and listed at Table IV.

It would be worthwhile helpful to compare the absolute value of the dominant component $|\chi^{(2)}_{322}(\omega)|$ (Fig. 4(b), upper panel) with the absorptive part of the corresponding dielectric function $\varepsilon_2(\omega)$ as a function of both $\omega/2$ and ω (Fig. 4(b), lower panel). The first structure $|\chi^{(2)}_{322}(\omega)|$ between 1.94 and 3.7 eV is mainly originated from 2ω resonance [see $\varepsilon_2(\omega/2)$; Fig. 4(b), lower panel]. The second structure between 3.7 and 8.0 eV is associated with interference between 2ω and ω resonances (the threshold of $\varepsilon_2(\omega)$) [see $\varepsilon_2(\omega/2)$ and $\varepsilon_2(\omega)$; Fig. 4(b), lower panel]. The last spectral structure (within 8.0–11.0 eV) is mainly due to ω resonance and is associated with the second structure in $\varepsilon_2(\omega)$.

TABLE IV. The SHG coefficients of some well-known NLO crystals at $\lambda = 1.064$ μm (unit: pm/V, where 1 pm/V $= 2.387 \times 10^{-9}$ esu).

Crystal	d_{ij}	Theory (pm/V)	Expt. (pm/V)
$KTiOPO_4$ (KTP)	d_{31}	2.7[a]	2.71[a], 2.54[b],
	d_{32}	4.85[a]	4.79[a], 4.35[b],
	d_{33}	16.75[a]	16.65[a],16.9[b],
KH_2PO_4 (KDP)	d_{36}		0.39[c]
	d_{31}		4.4[c]
$C_3H_7O_2N$	d_{14}	0.48[d]	0.56[d]
	d_{25}	0.16[d]	0.12[d]
	d_{36}	0.38[d]	0.21[d]
$KNbO_3$	d_{31}		−11.9[d]
	d_{32}		−13.7[d]
	d_{33}		−20.6[d]
$BaBiBO_4$	d_{15}	0.51[d]	0.40[d]
	d_{24}	1.13[d]	1.10[d]
	d_{33}	0.13[d]	0.15[d]
β-BaB_2O_4 (BBO)	d_{22}		±2.3[d]
	d_{31}		±0.16[d]
LiB_3O_5 (LBO)	d_{31}		±0.67[d]
	d_{32}		±0.85[d]
	d_{33}		±0.04[d]
CsB_3O_5	d_{14}		1.49[d]
$LiNaB_4O_7$	d_{15}	0.0219[e]	
	d_{24}	0.0481[e]	
	d_{31}	0.0733[e]	
	d_{32}	0.0795[e]	
	d_{33}	0.0136[e]	

[a]Reference 35.
[b]Reference 58.
[c]Reference 59.
[d]Reference 36.
[e]Reference of this work.

Fig. 4(c) shows that the second-order nonlinear optical susceptibility is very sensitive to the scissors' correction. The scissors' correction has a profound effect on magnitude and sign of $\chi^{(2)}_{ijk}(\omega)$.[48,49] The well-known LDA and GGA underestimation of the energy band gaps may result in incorrect values of second-order nonlinear optical susceptibility tensor components since they are more sensitive to the band gaps than the linear-response values due to higher power energy differences in the denominators of the formulae of complex second-order nonlinear optical susceptibility tensors [see Eqs. (6)–(8)]. In order to reduce the effect of the scissors' correction, we have used the EVGGA and mBJ approaches and we found that mBJ brings the gap closer the experimental one.

In Fig. 4(d), we show the imaginary and real parts of the dominate component which show that the imaginary and real parts of the second harmonic generation susceptibility are zero below half the energy band gap. The 2ω terms begin to contribute at energies $\sim 1/2E_g$ and the ω terms for energy values above E_g. At low spectral range ($\leq$1.94 eV), the SHG optical spectra are dominated by the 2ω contributions.

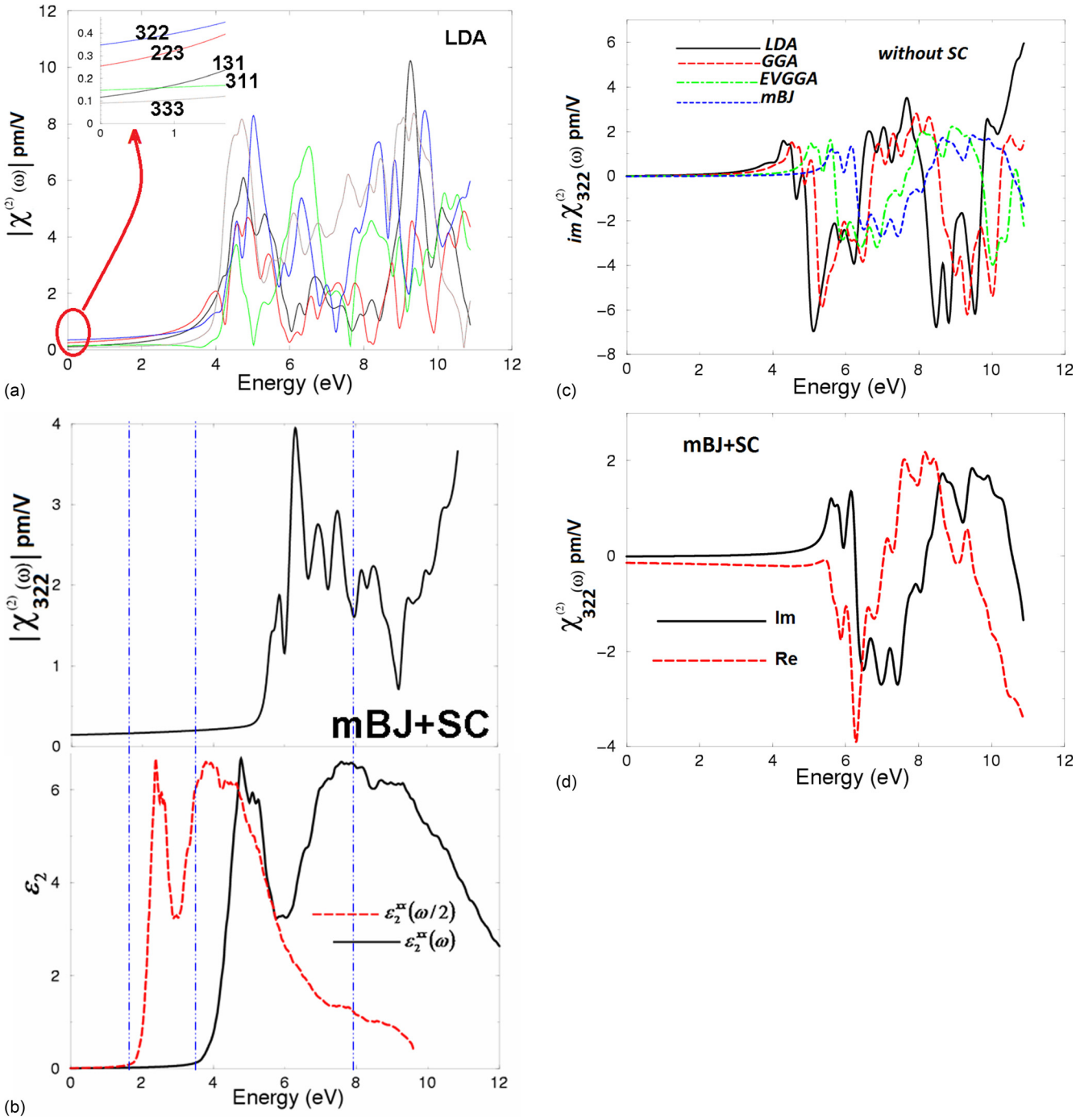

FIG. 4. (a) Calculated $|\chi^{(2)}_{ijk}(\omega)|$ for the five components with scissors correction. (b) Upper panel: calculated $|\chi^{(2)}_{322}(\omega)|$ (dark solid curve-black) using mBJ with scissors correction; Lower panel: calculated $\varepsilon_2^{xx}(\omega)$ (dark solid curve-black); calculated $\varepsilon_2^{xx}(\omega/2)$ (dark dashed curve-red). (c) Calculated imaginary part of the dominant components $\chi^{(2)}_{322}(\omega)$ for LDA, GGA, EVGGA, and mBJ without scissors correction. (d) Calculated imaginary $\chi^{(2)}_{322}(\omega)$ (dark solid curve-black) and real $\chi^{(2)}_{322}(\omega)$ (light dashed curve-red) spectra, using mBJ with scissors correction.

Beyond 3.88 eV (values of the fundamental energy gaps), the major contribution comes from the ω term. To the best of our knowledge, there are no experimental data for NLO susceptibilities of the title compound, which are available in the literatures to compare with our theoretical results. We would like to mention here that in our previous works[50–56] we have calculated the linear and nonlinear optical susceptibilities using FPLAPW method on several systems whose linear and nonlinear optical susceptibilities are known experimentally. We find very good agreement with the experimental data. Thus, we believe that our calculations reported in this paper would produce very accurate and reliable results. Furthermore, for the application of title NLO crystal, we have listed in Table IV, some values of the tensor components for some well-know NLO crystals along with the tensor components of the title crystal.

From the calculated $\chi^{(2)}_{ijk}(\omega)$ dispersion, we have obtained the microscopic second order hyperpolarizability, β_{ijk}, the vector components along the dipole moment direction. The microscopic second order hyperpolarizability terms

cumulatively yield a bulk observable second order susceptibility term, $\chi^{(2)}_{ijk}(\omega)$, which in turn is responsible for the high SHG response.[47,57] For the dominant component $|\chi^{(2)}_{322}(\omega)|$, we have calculated β_{322} at the static limit and at $\lambda = 1064$ nm, using the expression given in Ref. 47:

$$\beta_{ijk} = \frac{\chi^{(2)}_{ijk}}{Nf^3}, \tag{9}$$

where N is the number of molecules/cm^3 and f is the local field factor, the value of f is varying between 1.3 and 2.0. Using this information, we can estimate the value of first order hyperpolarizability tensor β_{ijk}. Following Eq. (9), the value of β_{322} is equal to 0.306×10^{-30} esu at static limit and 0.332×10^{-30} esu at $\lambda = 1064$ nm.

IV. CONCLUSIONS

The noncentrosymmetric borate with the composition $LiNaB_4O_7$ has been synthesized and characterized. It contains $[B_4O_9]^{6-}$ groups composed of two vertex-sharing BO_4 tetrahedra and two bridging BO_3 triangles as the basic structural units that are condensed through the nonbridging O atoms to produce a 3D network, with the intersecting channels hosting the Na^+ and Li^+ cations. The optical properties have been investigated in terms of diffuse reflectance spectra, which reveal the presence of an optical gap of 3.88 eV. Linear and nonlinear optical susceptibilities have been calculated for this compound. We have optimized the atomic positions taken from our XRD data by minimizing the forces. We employed the state-of-the-art all-electron FP-LAPW method to solve the Kohn Sham equations. The linear optical susceptibilities show that the title crystal possesses a wide optical gap of about 2.80, 2.91, 3.21, and 3.81 eV using LDA, GGA, EVGGA, and mBJ, respectively. This compares well with our experimentally measured energy band gap of 3.88 eV. Our calculations show that EVGGA and mBJ cause a blue spectral shift with significant changes in the whole spectra. The observed spectral shifts are in agreement with the calculated band structure and corresponding electron density of states. The tensor $\chi^{(2)}_{ijk}$ describes the second-order nonlinear optical effect and the symmetry allows only five nonzero components, namely, the 113, 232, 311, 322, and 333 components. The 322 component is dominant. For the dominant component, we have obtained the microscopic second order hyperpolarizability, β_{322}, to be about 0.306×10^{-30} esu at static limit and 0.332×10^{-30} esu at $\lambda = 1064$ nm.

ACKNOWLEDGMENTS

For Ali H. Reshak, this work was supported from the program RDI of the Czech Republic, the project CENAKVA (No. CZ.1.05/2.1.00/01.0024), the Grant No. 152/2010/Z of the Grant Agency of the University of South Bohemia and School of Material Engineering, Malaysia University of Perlis, P.O. Box 77, d/a Pejabat Pos Besar, 01007 Kangar, Perlis, Malaysia. For X. Chen, the work was supported from the National Natural Science Foundation of China (Grant No. 20871012). S. Auluck would like to thank the National Physical Laboratory for the J. C. Bose Fellowship.

[1] P. Becker, Adv. Mater. (Weinheim, Ger.) **10**, 979 (1998).
[2] J. Liebertz, Z. Krystallogr. **158**, 319 (1982); J. Liebertz and S. Stahr, Z. Kristallogr. **165**, 91 (1983).
[3] Z. Weizhuo, H. Huicong, L. Zhiping, Z. Thiande, H. Sukun, T. Dingyuan, and Z. Qinglan, Sci. China, (Ser. B) **38**(2), 145 (1995).
[4] P. Becker, J. Liebertz, and L. Bohaty, J. Cryst. Growth **203**, 149 (1999).
[5] A. A. Kaminskii, P. Becker, L. Bohaty, K. Ueda, K. Takaichi, J. Hanuza, M. Maczka, H. J. Eichler, and M. A. Gad, Opt. Commun. **206**, 179 (2002); M. Burianek, P. Held, and M. Muhlberg, Cryst. Res. Technol. **37**, 179 (2002).
[6] M. Burianek, P. Held, and M. Muhlberg, Cryst. Res. Technol. **37**, 785 (2002).
[7] S. Filatov, Y. Shepelev, R. Bubnova, N. Sennova, A. V. Egorysheva, and Y. F. Kargin, J. Solid State Chem. **177**, 515 (2004); H. Hellwig, J. Liebertz, and L. Bohaty, Solid State Commun. **109**(4), 249 (1998); M. Ghotbi, M. Ebrahim-Zadeh, A. Majchrowski, E. Michalski, and I. V. Kityk, Opt. Lett. **29**, 2530 (2004); M. Ghotbi, Z. Sun, A. Majchrowski, E. Michalski, and I. V. Kityk, Appl. Phys. Lett. **89**, 173124 (2006).
[8] E. M. Levin and C. L. McDaniel, J. Am. Ceram. Soc. **45**, 355 (1962).
[9] Y. F. Kargin and A. V. Egorysheva, Inorg. Mater. **34**, 714 (1998).
[10] A. Hyman and A. Perloff, Acta Crystallogr., Sect. B: Struct. Crystallogr. Cryst. Chem. **28**, 2007 (1972).
[11] R. Frohlich, L. Bohaty, and J. Liebertz, Acta Crystallogr., Sect. C: Cryst. Struct. Commun. **40**, 343 (1984).
[12] B. Teng, W. T. Yu, J. Y. Wang, X. F. Cheng, S. M. Dong, and Y. G. Liu, Acta Crystallogr., Sect. C: Cryst. Struct. Commun. **58**, 125 (2002).
[13] M. Muehlberg, M. Burianek, H. Edongue, and C. Poetsch, J. Cryst. Growth **237**, 740 (2002).
[14] A. V. Egorysheva, V. I. Burkov, V. S. Gorelick, Yu. F. Kargin, V. V. Koltashev, and B. G. Plotnichenko, Fiz. Tverd. Tela (St. Petersburg) **43**, 1590 (2001); Phys. Solid State **43**, 1655 (2001).
[15] G. Blasse, E. W. J. L. Oomen, and J. Liebertz, Phys. Status Solidi B **137**, K77 (1986).
[16] S. Haussühl, L. Bohatý, and P. Becker, Appl. Phys. A: Mater. Sci. Process. **82**, 495 (2006).
[17] A. Brenier, I. V. Kityk, and A. Majchrowski, Opt. Commun. **203**, 125 (2002); A. Majchrowski, J. Kisielewski, E. Michalski, K. Ozga, I. V. Kityk, and T. Lukasiewicz, Opt. Commun. **250**, 334 (2005); I. V. Kityk and A. Majchrowski, Opt. Mater. **26**, 33 (2004).
[18] B. Teng, J. Wang, Z. Wang, H. Jiang, X. Hu, R. Song, H. Liu, Y. Liu, J. Wei, and Z. Shao, J. Cryst. Growth **224**, 280 (2001).
[19] Z. Wang, B. Teng, K. Fu, X. Xu, R. Song, C. Du, H. Jiang, J. Wang, Y. Liu, and Z. Shao, Opt. Commun. **202**, 217 (2002); A. H. Reshak, S. Auluck, I. V. Kityk, A. Majchrowski, D. Kasprowicz, M. Drozdowski, J. Kisielewski, T. Lukasiewicz, and E. Michalski, J. Mater. Sci. **41**, 1927 (2006).
[20] Z. Lin, Z. Wang, C. Chen, and M. H. Lee, J. Appl. Phys. **90**, 5585 (2001).
[21] D. Xue, K. Betzler, H. Hesse, and D. Lammers, Solid State Commun. **114**, 21 (2000).
[22] J. Barbier, N. Penin, A. Denoyer, and L. M. D. Cranswick, Solid State Sci. **7**, 1055 (2005).
[23] J. Barbier, N. Penin, and L. M. Cranswick, Chem. Mater. **17**, 3130 (2005).
[24] J. Barbier and L. M. D. Cranswick, J. Solid State Chem. **179**, 3958 (2006).
[25] M. Maczka, A. Waskowska, A. Majchrowski, J. Zmija, J. Hanuza, G. A. Peterson, and D. A. Keszler, J. Solid State Chem. **180**, 410 (2007).
[26] S. Gao, Comput. Phys. Commun. **153**, 190 (2003).
[27] K. Schwarz, J. Solid State Chem. **176**, 319 (2003).
[28] G. M. Sheldrick, SHELX-97: Program for Structure Refinement, University of Goettingen, Germany, 1997.
[29] J. Li, Z. Chen, X.-X. Wang, and D. M. Proserpio, J. Alloys Compd. **28**, 262 (1997).
[30] W. W. M. Wendlandt and H. G. Hecht, *Reflectance Spectroscopy* (Interscience, New York, 1966).
[31] P. Blaha, K. Schwarz, G. K. H. Madsen, D. Kvasnicka, and J. Luitz, *WIEN2K: An Augmented Plane Wave + Local Orbitals Program for Calculating Crystal Properties* (Karlheinz Schwarz, Techn. Universitat, Wien, Austria, 2001).
[32] P. Hohenberg and W. Kohn, Phys. Rev. B **136**, 864 (1964).
[33] D. M. Ceperley and B. I. Ader, Phys. Rev. Lett. **45**, 566 (1980); parametrized in J. P. Perdew and A. Zunger, Phys. Rev. B **8**, 4822 (1973).
[34] J. P. Perdew, S. Burke, and M. Ernzerhof, Phys. Rev. Lett. **77**, 3865 (1996).

[35]E. Engel and S. H. Vosko, Phys. Rev. B **47**, 13164 (1993).
[36]F. Tran and P. Blaha, Phys. Rev. Lett. **102**, 226401 (2009).
[37]F. Bassani and G. P. Parravicini, *Electronic States and Optical Transitions in Solids* (Pergamon, Oxford, 1975), pp. 149–154.
[38]F. Wooten, *Optical Properties of Solids* (Academic, New York, 1972).
[39]R. H. French, H. Mullejans, and D. J. Jones, J. Am. Ceram. Soc. **81**, 2549 (1998).
[40]S. Sharma, J. K. Dewhurst, and C. Ambrosch-Draxl, Phys. Rev. B **67**, 165332 (2003); S. Sharma and C. Ambrosch-Draxl, Physica T **109**, 128 (2004).
[41]A. H. Reshak, Ph.D. thesis, Indian Institute of Technology-Rookee, India, 2005.
[42]A. H. Reshak, J. Chem. Phys. **125**, 014708 (2006); **124**, 014707 (2006).
[43]S. N. Rashkeev and W. R. L. Lambrecht, Phys. Rev. B **63**, 165212 (2001); S. N. Rashkeev, W. R. L. Lambrecht, and B. Segall, *ibid.* **57**, 3905 (1998).
[44]C. Ambrosch-Draxl and J. Sofo, Comput. Phys. Commun. **175**, 1–14 (2006).
[45]D. E. Aspnes, Phys. Rev. B **6**, 4648 (1972).
[46]J. F. Nye, *Physical Properties of Crystals* (Clarenndon, Oxford, 1967).
[47]R. W. Boyd, *Principles of Nonlinear Optics* (Academic Press, NY, 1982), p. 420.
[48]A. H. Reshak and S. Auluck, Physica B **388**, 34 (2007).
[49]A. H. Reshak, S. Auluck, and I. V. Kityk, Appl. Phys. A **91**, 451 (2008).
[50]A. H. Reshak, S. Auluck, and I. V. Kityk, J. Phys.: Condens. Matter **20**, 145209 (2008).
[51]A. H. Reshak, S. Auluck, and I. V. Kityk, J. Solid State Chem. **181**, 789–795 (2008).
[52]A. H. Reshak, J. Chem. Phys. **124**, 104707 (2006).
[53]A. H. Reshak, Eur. Phys. J. B **47**, 503–508 (2005).
[54]A. H. Reshak, I. V. Kityk, and S. Auluck, J. Phys. Chem. B **114**, 16705–16712 (2010).
[55]A. H. Reshak, S. Auluck, D. Stys, I. V. Kityk, H. Kamarudin, J. Berdowski, and Z. Tylczynskif, J. Mater. Chem. **21**, 17219 (2011).
[56]A. H. Reshak, M. Piasecki, S. Auluck, I. V. Kityk, R. Khenata, B. Andriyevsky, C. Cobet, N. Esser, A. Majchrowski, M. S'wirkowicz, R. Diduszko, and W. Szyrski, J. Phys. Chem. B **113**(46), 15237 (2009).
[57]R. W. Boyd, *Nonlinear Optics*, 3rd ed. (Acadmic Press is an imprint of Elsevier, 2008).
[58]K. Zhang and X. Wang, Chin. Sci. Bull. **46**, 2028–2036 (2001).
[59]Data taken from V. G. Dmitriev, G. G. Gurzadyan, and D. N. Nikogosyan, *Handbook of Nonlinear Optical Crystals*, 3rd revised ed. (Springer-Verlag, Berlin, 1999).